ELSEVIER

A carbonate-free, sulfone-based electrolyte for high-voltage Li-ion batteries

Judith Alvarado [1,2,†], Marshall A. Schroeder [1,†], Minghao Zhang [2], Oleg Borodin [1], Eric Gobrogge [1], Marco Olguin [1], Michael S. Ding [1], Mallory Gobet [3], Steve Greenbaum [3], Ying Shirley Meng [2,*], Kang Xu [1,*]

[1] Electrochemistry Branch, Sensors and Electron Devices Directorate, U.S. Army Research Laboratory, Adelphi, MD 20783, USA
[2] Materials Science and Engineering, University of California, San Diego, La Jolla, CA 92093, USA
[3] Department of Physics and Astronomy, Hunter College, City University of New York, New York, NY 10065, USA

Practical implementation of next-generation Li-ion battery chemistries is to a large extent obstructed by the absence of an electrolyte that is capable of simultaneously supporting reversible electrochemical reactions at two extreme electrochemical potentials—above 4.5 V at the positive electrode and near 0 V vs. Li at the negative electrode. Electrolytes based on carbonate esters have been reliable in satisfying state-of-the-art Li-ion battery (LIB) chemistries below <4.2 V; however, it is the intrinsic thermodynamic tendency of these carbonates to decompose at potentials well below the thermodynamic threshold required for reversible reactions of high-voltage systems (>4.4 V), releasing CO_2. In this work, we explore a carbonate-free electrolyte system based on a single sulfone solvent, in which a newly discovered synergy between solvent and salt simultaneously addresses the interfacial requirements of both graphitic anode and high-voltage cathode ($LiNi_{0.5}Mn_{1.5}O_4$ (LNMO)). Experimental measurements, quantum chemistry (QC) calculations, and molecular dynamics simulations reveal the system's fast ion conduction, stability over a wide temperature range, and non-flammability. At the anode, a LiF-rich interphase generated by early-onset reduction of the salt anion effectively suppresses solvent co-intercalation and subsequent graphite exfoliation, enabling unprecedented and highly reversible graphite cycling in a pure sulfone system. Under oxidative conditions, QC calculations predict that high salt concentration promotes complex/aggregate formation which slow the decomposition of sulfolane and leads to polymerizable rather than gaseous products—a fundamental improvement over carbonate solvents. These predictions are corroborated by X-ray photoelectron spectroscopy (XPS), cryogenic-transmission electron microscopy (TEM), and electron energy loss spectroscopy (EELS) experiments, which revealed the presence of a thin, conformal, sulfur-based cathode electrolyte interphase (CEI). Together, the functional interphases (SEI/CEI) generated by this electrolyte system

---

* Corresponding authors.
  E-mail address: Xu, K. (conrad.k.xu.civ@mail.mil)
  † J.A. and M.S. contributed equally to this work.

supported long term operation of a high-voltage (4.85 V) LNMO/graphite full cell, which retained ~70% of its original first-cycle discharge capacity after the 1000th cycle. Based on these results, this new carbonate-free electrolyte system, supported by the mechanistic understanding of its behavior, presents a promising new direction toward unlocking the potential of next generation Li-ion battery electrodes.

Introduction

Since the initial commercialization of lithium ion batteries (LIBs) more than 25 years ago, the energy demands of portable electronic devices have rapidly outpaced the deliverable performance metrics of state-of-the-art LIB. This already widening gap is further strained by the recent surge in development and adoption of large-scale energy storage applications including electric vehicles and smart electric grids. These systems bring increasingly stringent requirements for energy/power densities, cycle life, low cost, and safety. An assortment of energy dense, high-voltage cathode materials including $LiNi_{0.5}Mn_{1.5}O_4$ (LNMO), $LiCoPO_4$ (LCP), and layered Li–Ni–Mn–Co oxides (NMC) offer promising theoretical performance metrics; however, the accompanying challenges that primarily arise from the currently available carbonate-based electrolytes must be addressed.

The first of these challenges has troubled Li-ion battery development from the start: achieving reversible lithium intercalation chemistry at extremely low potentials (~0 V vs. Li) while preventing persistent decomposition of electrolyte components (solvents and anions). The key enabler of this process in commercial Li-ion cells is the solid-electrolyte-interphase (SEI) [1], which forms as a result of self-limited decomposition reactions of electrolyte components and ultimately dictates the reversibility and kinetics of lithium intercalation on the anode [2,3]. The SEI is extremely sensitive to the electrolyte composition (solvent, salt and its concentration) as well as formation conditions. Despite extensive investigation of many aprotic solvents and additives, only ethylene carbonate (EC) [4] and a few other "enablers" (vinylene carbonate (VC) [5], fluoroethylene carbonate (FEC), (4R,5S)-4,5-difluoro-1,3-dixolan-2-one [6] (DiFEC), methylene-ethylene carbonate [7] (MEC), prop-1-ene-1,3-sultone [8] (PES), and succinic anhydride [9] (SA)) have been reported to exhibit this behavior. Aside from this limited group, most other electrolyte systems (particularly non-carbonate systems) demonstrate similar electrochemical behaviors to propylene carbonate (PC), which undergoes extensive irreversible reduction and exfoliates the graphitic structure. The SEI consideration is the primary motivation for the exclusive use of carbonate-based electrolytes in commercial LIBs.

The second major challenge has emerged more recently with the development of high-voltage cathode materials, which offer greater energy density at the expense of exposing electrolytes to more aggressive electrochemical conditions. The performance of these electrodes in conventional carbonate-based electrolytes suffers from extensive degradation at or above 4.4 V due to continuous oxidation processes which occur as a result of a combination of intrinsic thermodynamic limitations and highly reactive cathode surfaces and defects. These processes result in CO_2 generation, active material consumption, and increased cell impedance [10]—all of which accelerate at elevated temperatures [11–15]. While numerous non-carbonate electrolyte systems with superior anodic stability such as nitriles, sulfones, ionic liquids, and fluorinated carbonates have been tested with these new cathode materials and achieved certain success, they often fail to form a suitable anode SEI, leading to graphite exfoliation and limited practical use in full cells. Conversely, SEI-forming additives can be used to assist these non-carbonate solvents, but most of them are anodically unstable against high-voltage cathode surfaces, leading to participation in the same type of parasitic reactions they are added to suppress.

Here, we report a two component electrolyte formulation that reconciles both of these challenges without requiring additives. Tetramethylene sulfone, or sulfolane (SL), is a highly polar aprotic solvent with high thermal and voltage stability windows when used as bulk electrolyte solvent. When used in combination with lithium bis(fluorosulfonyl)imide (LiFSI), a highly conductive lithium salt with an anion that has strong tendency to donate fluorine, this simple electrolyte exhibits synergistic interphase formation mechanisms (CEI/SEI). Together, these interphases enable stable coupling of a graphitic anode and a high-voltage cathode over an extended temperature range.

Results and discussion

Bulk and transport properties

The temperature-dependences of conductivity for 1.0 m (mol kg^{-1}) and 3.25 m LiFSI in SL are shown in Fig. 1a, with 1.0 m $LiPF_6$ in EC/EMC (3:7) (Gen II) for comparison [16]. LiFSI-SL system exhibits approximate conductivities of 2–3 mS cm^{-1} depending on the concentration, less than an order of magnitude lower than the standard carbonate formulations despite viscosity penalties associated with the solvent and increased salt concentration. Part of the conductivity penalty is compensated by the higher apparent Li+-transference number (t^+), which can be estimated from ion self-diffusion coefficients. The pfg–NMR (and MD simulations) yield $t^+ = 0.48$ (0.48 MD) for 1 m LiFSI–SL and 0.58 (0.65 MD) for 3.25 m LiFSI, much higher than the mixed carbonates $t^+ = 0.24$–0.34 ($LiPF_6$/EC/DEC) [17] and $t^+ \approx 0.4$ for ($LiPF_6$/EC:DMC) [18]. Interestingly, at 3.25 m MD simulations and pfg–NMR predict that the Li+ diffusion is not only faster than diffusion of the FSI^- anion but also is faster than diffusion of SL solvent (Fig. S1), suggesting that the Li+ cation moves via solvent and anion exchange in 3.25 m LiFSI–SL. More detailed analysis of MD trajectories showed that during one Li+–SL residence time, a Li+ moves 6.4 Å and 7.4 Å for 1 m and 3.25 m LiFSI–SL, respectively. These distances are similar to the size of the SL molecule and FSI^- anion. Thus, a Li+ cation exchanges on average one solvent and anion from its solvation shell as it moves a distance equivalent to their size, further confirming the importance of solvent and anion exchange contributions to the Li+ diffusion. In contrast, MD simulations predict that in

EC:DMC (1:3) with 1 M LiPF$_6$, the Li$^+$ cation moves much longer distance of 11.4 Å before it exchanges a DMC solvent in its solvation shell, showing a larger contribution of the Li$^+$ vehicular transport with DMC. While enhancement of the exchange mechanism with increasing salt concentration was previously discussed for concentrated electrolytes [19–21], dominance of the exchange contribution is clear even in the low concentration 1 m LiFSI-SL electrolyte, which becomes supercooled 15 °C lower than 3.25 m LiFSI–SL (Fig. S2), but was slower to recover when reheated. Otherwise, no hysteresis was observed over the measured temperature range, indicating relatively fast kinetic processes.

These electrolytes were also characterized with differential scanning calorimetry (DSC) to establish a suitable temperature window of operation. The carbonate baseline exhibited a major endothermic behavior at 175 °C, where the DSC cell ruptured due to overpressure from gas generation (Fig. 1b). Conversely, the 3.25 m LiFSI–SL persisted until >280 °C before rupturing, suggesting less gas generation occurred over the majority of this extended temperature range, though the exothermic peaks above 200 °C do suggest certain chemical reactivity.

FTIR measurements were conducted on SL–FSI at various salt concentrations to study the Li$^+$-solvation behavior. Due to large amounts of spectral overlap, the solvation behavior was studied utilizing only two regions of the spectra containing features assigned primarily to the structure of SL molecule. The first is the SO$_2$ twist in SL, located at ~445 cm^{-1} [22,23]. This region can be deconvoluted into two components (dashed lines, Figs. 2a, S3). The feature centered at 440 cm^{-1} corresponds to the SO$_2$ twist of non-solvating SL molecules in the electrolyte.
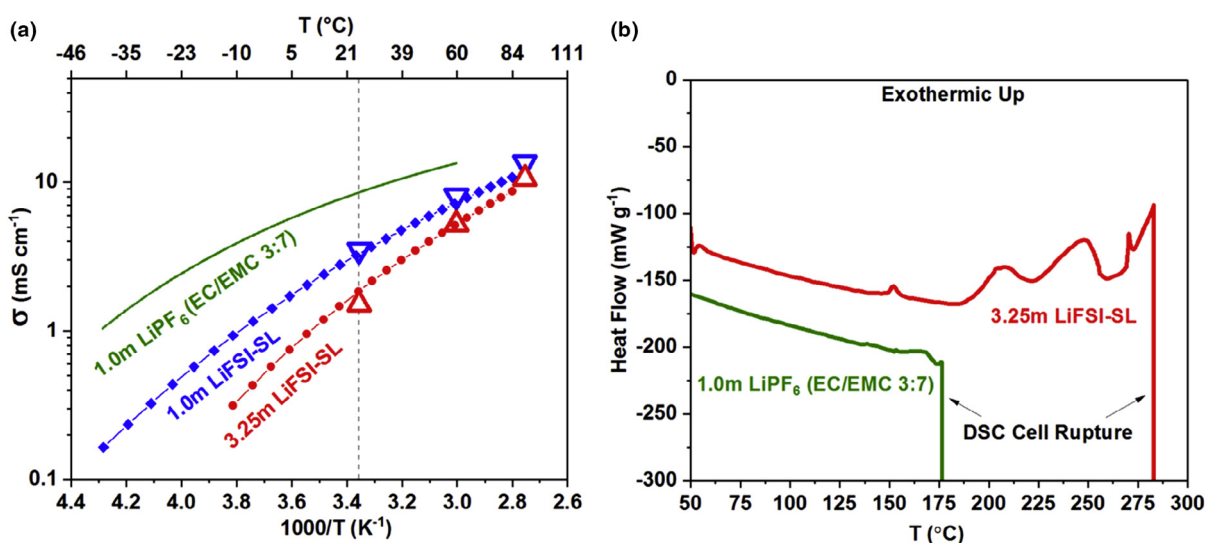

FIGURE 1

(a) Temperature-dependent conductivities for 1.0 m and 3.25 m LiFSI in SL as compared to 1.0 m LiPF$_6$ in EC/EMC (3:7). Open triangles indicate MD calculated values for the LiFSI-SL electrolytes. (b) DSC heat flow measurement of LiFSI-SL electrolytes with baseline carbonate electrolyte for comparison.
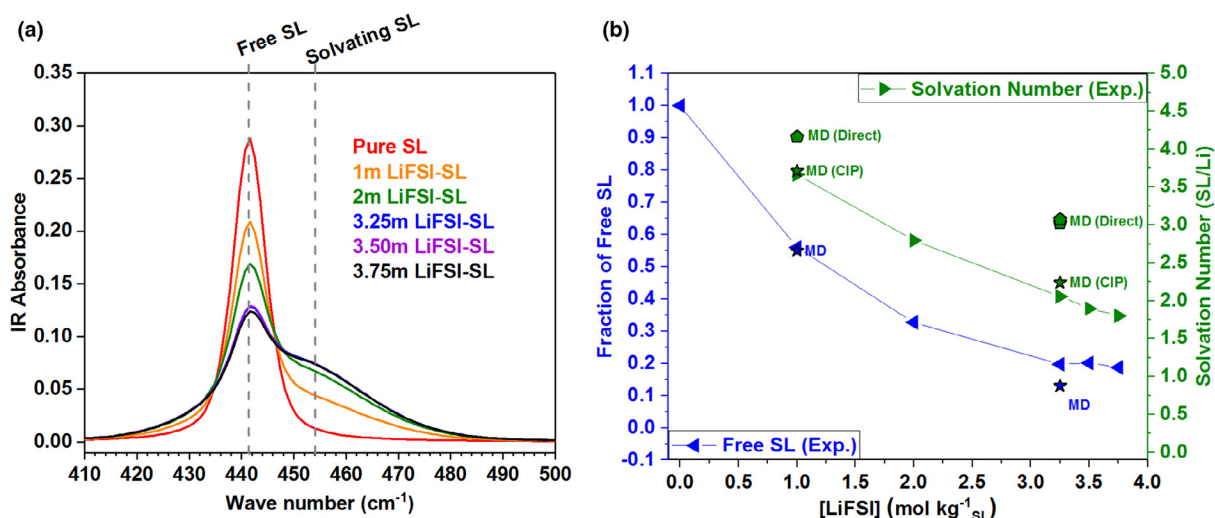

FIGURE 2

(a) FTIR spectra of sulfolane's SO$_2$ twist over a series of LiFSI concentrations. (b) The fraction of the free sulfolane (blue) and solvation number (green) as a function of concentration according to FTIR measurements and MD simulations.

This was confirmed by comparison to pure SL (Fig. S3a) and the broader feature at 450 cm^{-1} corresponds to the SO$_2$ twist of SL molecules coordinated with Li$^+$. With this deconvolution, the fractional area of both components can be tracked as a function of LiFSI concentration (Fig. 2b). As expected, the fraction of SL molecules participating in the solvation of Li$^+$ increase accordingly with LiFSI concentration. These observations are further supported by analysis of sulfolane's CH$_2$ spectral region (∼1100 cm^{-1}, Fig. S4) [22,23], which is discussed further in the Supporting Information. In Fig. 2b (blue), the fraction of free SL from MD simulations is also shown for comparison, and is in excellent agreement with the FTIR analysis. The average solvation number (N_S) of Li$^+$ is typically determined from the relation [24]:

$$\frac{A_{SL(Li)}}{A_{SL(Li)} + A_{SL(Free)}} = N_S \frac{c_{(Li)}}{c_{(SL)}}, \tag{1}$$

where $A_{SL(Li)}$ and $A_{SL(Free)}$ are the integrated area intensities of the bands for the SL coordinated by Li$^+$ and free SL not coordinated by Li, respectively. The $c(Li)$ and the $c(SL)$ correspond to the concentrations of the lithium cations and SL. This relation assumes that only one Li$^+$ can participate in the SL coordination forming contact ion pairs (CIP). Solvation numbers obtained from this CIP model are shown in Fig. 1b (green), indicating a drop from an average of 3.7 to 1.8 of SL per Li$^+$ as salt concentration increases from 1 m to 3.75 m. When this model (Eq. (1)) is applied to MD data by substituting the number of solvated and free SL instead of integrated intensities,

quite similar solvation numbers are obtained. However, when the Li$^+$ solvation numbers are calculated directly from MD simulations by analysis of the Li$^+$ solvation shell instead of using Eq. (1), significantly higher values were obtained. The discrepancy between direct calculation and CIP model prediction (Eq. (1)) is attributed to formation of extended short-lived aggregates where Li$^+$ bridges multiple SL molecules as shown in Fig. S5, as opposed to the single Li–SL CIP model. Therefore, a standard technique for extracting solvation numbers should not be used for solvents with multiple solvating groups, such as SL, that would allow multiple Li$^+$ coordinating a solvent. MD simulations also predicted the extent of ion aggregation. The LiFSI–SL electrolyte at 1 m is largely dissociated, consisting of 61% free SL and 33% contact ion pairs (CIPs), while the 3.25 m LiFSI–SL contains 47% of the FSI–Li CIPs and 43% of aggregates where FSI is coordinated by multiple Li$^+$. The FSI$^-$ aggregation state is important for LiF reduction and electron stabilization [25].

The Lithium graphite intercalation reaction

Sulfolane exhibits many attractive properties as an electrolyte solvent including excellent oxidative and high temperature stability, high dielectric constant, and acceptable stability toward lithium metal [26]. Unfortunately, selective separator wettability, electrolyte viscosity, and the inability to independently form a protective SEI on graphite have hindered its use as the primary electrolyte solvent [27,28]. The proposed LiFSI–SL electrolytes were tested in graphite–Li half cells with propylene carbonate-based electrolytes for comparison (Fig. 3 and Supporting Information for additional tests). In contrast to prior beliefs about sul-
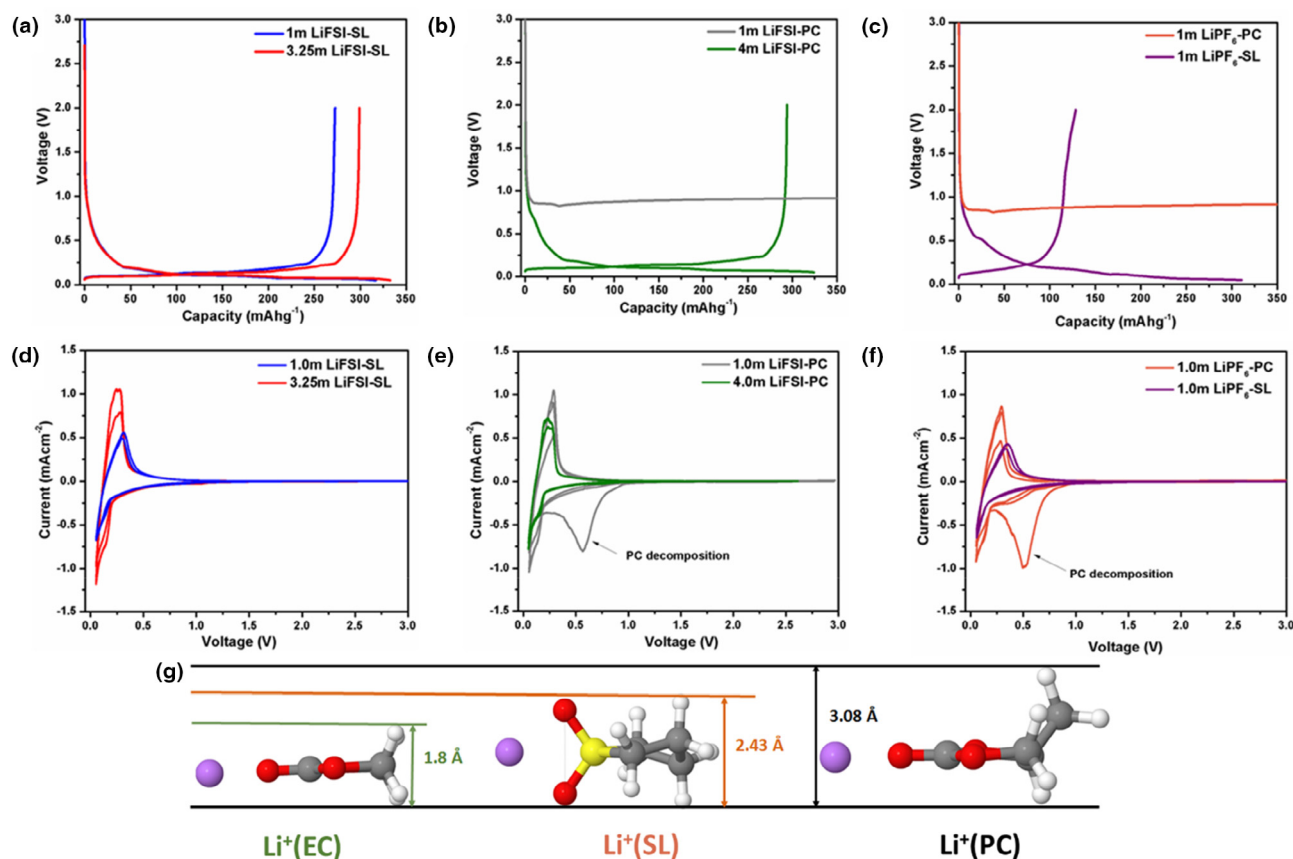

FIGURE 3

Galvanostatic cycling (a–c) and cyclic voltammetry (d–f) of MCMB graphite half cells at (a, d) 1.0 m and 3.25 m LiFSI SL, (b, e) 1.0 m and 4.0 m LiFSI PC, and (c, f) 1.0 m LiPF$_6$ PC and 1.0 m LiPF$_6$ SL. (g) Li-EC, Li-SL, and Li-PC co-intercalant structures with relative dimensions.

fones, the proposed LiFSI–SL electrolytes exhibit excellent galvanostatic cycling performance in graphite half cells, with a first cycle Coulombic efficiency (CE) of 85.9% for 1 m LiFSI–SL and 89.9% of 3.25 m LiFSI–SL. Especially in the latter case, a capacity of ~300 mAh/g is achieved for graphite, approaching the theoretical limit allowed by the stage I graphite intercalation (LiC_6, 372 mAh/g). The CE quickly increases to 99.8% for both high and low salt concentration electrolytes (Fig. S6). In sharp contrast and as expected, 1 m LiFSI–PC leads to severe graphitic exfoliation due to sustained electrolyte decomposition (Fig. 3b). Increasing the salt concentration to 4 m LiFSI in PC stabilizes the graphite anode with a new interphasial chemistry, and achieves an initial CE of 90.7% (Fig. 3b). This is consistent with the work by Nie et al. [29,30], and the performance improvement is attributed to the contribution of salt anion to the interphasial chemistry instead of solvent. Thus, graphite exfoliation can be prevented in LiFSI–SL system, regardless of salt concentration, while the PC system relies on high salt concentrations. To further detail the effect of salt anion versus that of solvent, SL and PC electrolytes with 1 m LiPF_6 were tested under identical conditions. Consistent with the literature [31], the PC electrolyte decomposes and exfoliates graphite with little contribution from the anion decomposition to SEI, while SL–LiPF_6 system presents certain reversibility but with only half of the graphite capacity, indicating the competitive interphasial chemistry from anion and solvent that will be dictated by Li^+-solvation structures.

While the precise mechanism of graphite exfoliation requires further exploration, the generally established cause is the excess strain generated by co-intercalation of the electrolyte solvent with Li^+ before an SEI is completely formed to enable Li^+ desolvation [32–35]. Logically, larger co-intercalates generate greater strain and more extensive exfoliation, leading to significant performance deterioration. This trend is supported by Fig. 3g, which compares the dimensions of EC–Li, SL–Li, and PC–Li co-intercalant structures. As an intermediate in size between the EC–Li (1.8 Å) and PC–Li (3.08 Å), the SL–Li (2.43 Å) co-intercalant likely generates less strain in the graphite compared to PC–Li, but more than EC–Li, supporting SL's intermediate interphasial behavior between the two, as reflected by the behavior observed in Fig. 3f at low salt concentrations. Of course, this explanation does not adequately address the reversible behavior observed for the 4 m LiFSI–PC and both LiFSI–SL systems, because the stability/instability of these intercalants against subsequent electrochemical reduction and the consequent products' adhesion to electrode surface would also determine whether the graphitic structure would be exfoliated or protected. Notably, reversible graphite cycling has been achieved with larger solvates including hindered glymes [36] and trans-2,3-butylene carbonate [37], but in both of these cases steric effects result in desolvation prior to exfoliation. In any of these cases, the reduction products ultimately define the chemistry, morphology and quality of the resulting SEI.

For the LiPF_6-based systems, the kinetic onset [38] for significant salt reduction and LiF formation generally occurs within the same potential range as reduction of PC and SL molecules (0.4–0.6 V vs. Li/Li^+, see Supporting information for more details), despite the fact that slow LiPF_6 salt reduction was observed [39] and predicted by QC calculations [40] to take place at higher potentials. This means Li-solvent co-intercalants have most likely entered and strained the graphitic structure before a sufficient amount of PF_6^- is reduced and can significantly contribute to SEI formation. Conversely, LiFSI reduction is energetically favorable at higher potentials, starting around 2.4 V vs. Li/Li^+ according to QC calculations (Fig. S15), the experiments in this work (Fig. S7), and previous studies with other solvents [25]. This will drive anion decomposition at higher potentials, potentially resulting in formation of an inorganic SEI prior to Li co-intercalation and the onset of exfoliation. While this effect enables the LiFSI–SL system across all concentrations tested, higher concentrations appear to be a necessary condition for reversible operation of the LiFSI–PC system. We attribute this high concentration requirement for the PC system to two effects: (1) the highly concentrated LiFSI–PC electrolyte is expected to further reduce the solubility of reduction products [41] such as LiF, thus making an SEI denser, and (2) raising concentration increases the populations of CIPs and aggregates needed to promote FSI decomposition at higher potentials, thus reducing the fraction of co-intercalants and minimizing graphitic strain. It is worth noting that the effect of LiPF_6 concentration was not further explored because of its room temperature solubility limit at 1.5 m. Notably, these findings add a significant caveat to the works by Yamada et al. [42,43], which suggest that significant concentrations of LiFSI are necessary for universalization of the graphite electrode in solvents other than EC, including sulfones.

Electrochemical impedance spectroscopy (EIS) was conducted on Li–MCMB graphite half-cells containing these electrolyte systems (Fig. S8, Tables S3 and S4). After the first lithiation (Table S3), a lower internal cell resistance was obtained for SL electrolytes as compared to the cells cycled in 4 m LiFSI–PC. The stark difference in these cells arises after the first delithiation (Table S4), during which cells with SL maintain a low charge-transfer resistance (R_{CT}) (4.25 Ω for 1 m LiFSI and 13.55 Ω for 3.25 m LiFSI), as compared 123.7 Ω for 4 m LiFSI–PC. The very minor R_{CT} dependence on concentration and lithiation state for the FSI–SL electrolytes supports the presence of an efficiently formed, stable and ionically conductive SEI which enables the reversible lithium intercalation/de-intercalation observed experimentally.

To ensure that SEI formation has been completed, MCMB graphite electrodes were galvanostatically cycled to the fifth lithiated cycle, and the electrodes were subsequently extracted from the cells and analyzed with XPS. Rigorous protocols were followed in order to prevent air exposure as described in the experimental section. The as-prepared graphite anode shows the characteristic peaks in the C1s associated with graphite, conductive additive, and PVDF binder (Fig. S9), and the cycled electrodes were subjected to high resolution region scans of C 1s, O 1s, F 1s, S 2p, N 1s, and Li 1s to identify the SEI chemistry. All of the XPS peak fits are found in the Supporting information with a detailed discussion (Figs. S7–S12).

Although SL has been considered as a potential solvent platform for high-voltage systems, to our knowledge there has been no experimental effort to determine its decomposition products on the negative electrode. Fig. 4a shows the normalized O1s spectra for the electrodes cycled in SL- and PC-based electrolytes at different salt concentrations. Both LiFSI–SL electrolytes show a
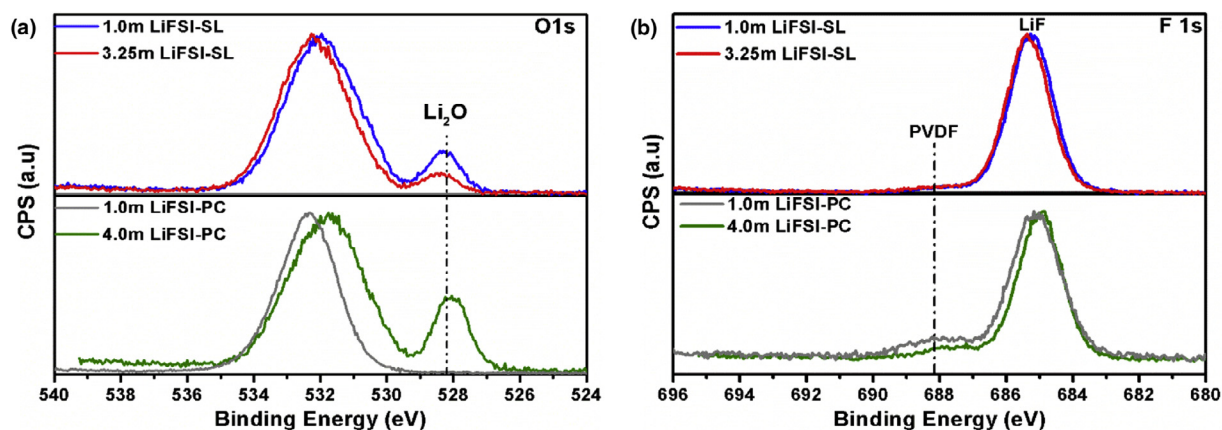
FIGURE 4

(a) O1s and (b) F1s comparison between FSI-SL and FSI-PC.

large peak at 532.2 eV, which is associated to the S—O bond potentially resulting from either SL or FSI^- decomposition. Furthermore, these electrodes also share a common peak at 528.38 eV corresponding to lithium oxide (Li_2O) [44–49]. For 1.0 m LiFSI–PC, the typical decomposition products of carbonates are found at 531.7 eV (C—O), 532.4 eV (O—C=O), and 533.1 eV (CO_3) (Fig. S10), with no presence of Li_2O peak. At 4.0 m concentration, however, it does exist, revealing the concentration-dependence of Li_2O-formation. To determine if its origin is from the anion (FSI^-) or solvent (SL), graphite half cells were cycled with two reference electrolytes: 1.2 m LiFSI–EC:EMC (3/7 v/v) to test the anion-dependent surface chemistry independent of SL, and 1.0 m $LiPF_6$–SL to test the solvent-based surface chemistry independent of the FSI^- anion. The cell with the LiFSI–carbonate electrolyte displayed signatures of Li_2O in the SEI (Fig. S10), while the SL containing $LiPF_6$ did not, indicating that Li_2O-formation originates from LiFSI rather than SL decomposition. QC calculations also show an energetically favorable pathway to Li_2O formation as a result of LiFSI reduction (Fig. S15) [50–52]. Interestingly, the previous literature does not specifically identify Li_2O in the SEIs formed by LiFSI. Nie et al. studied the role of LiFSI on the SEI formation using EC, but did not report any Li_2O on the graphite surface [53]. Philippe and coworkers showed that when LiFSI was used to cycle a silicon anode, the presence of Li_2O resulted from the reaction between Li^+ and SiO_2, instead from salt decomposition [54]. While researchers have not been able to directly link the presence of Li_2O to LiFSI decomposition, we confirmed this connection, and believe that Li_2O, as one of the final decomposition products from LiFSI reduction, may be a critical component for LiFSI-based SEI on graphite.

The F 1s spectra were normalized using the electrode's PVDF binder as reference to quantify F-containing SEI decomposition products. The large peak at 685 eV corresponds to LiF due to the LiFSI reduction—seen in both SL and PC electrolytes. This is expected since both computational and empirical measurements propose rapid defluorination of LiFSI to form LiF under reducing conditions [55–57]. The relative concentration of LiF and PVDF differs significantly for each electrolyte solvent and concentration. For electrodes cycled in both low and high

concentration LiFSI–SL electrolytes, the percent concentration of LiF to PVDF was ~96.60% and 3.40%, respectively. Conversely, the electrode cycled with 1.0 m LiFSI–PC has 86.71% LiF and 13.29% PVDF. This ratio increases only slightly in the case of high concentration (4.0 m LiFSI–PC, LiF: 91.84%, PVDF: 8.16%). The detailed fits are shown in the Supporting Information without count normalization. These results indicate that LiFSI–SL electrolytes lead to an SEI strongly based on the FSI^- anion, with a significant presence of inorganic species including Li_2O and LiF, while PC-electrolytes, especially at low concentration, still consist of a significant portion of solvent reduction products.

We propose that SEI formation is initiated at high voltages (>2 V vs. Li/Li^+) as a result of LiFSI reduction, leading to LiF and eventually Li_2O formation that constitutes the initial SEI products [50–52]. SL reduction occurs at the later stages of the formation cycle at ~0.4 V, contributing to the SO_2-rich SEI that is consistent with QC results (Fig. S16). As expected, the SEI surface chemistry appears to be a key factor in improving the electrochemical window and cycling stability as compared to the PC electrolytes.

Oxidative stability

The oxidative stability of SL has been examined previously with both experimental measurements [58–60] and theoretical calculations [61–63], which collectively suggest a decomposition threshold at or above 5.0 V vs. Li. While the instability of the anion in an electrolyte can significantly suppress the anodic stability of the entire electrolyte [40], Wang et al. recently demonstrated that LiFSI can also be successfully applied to high-voltage systems (4.6 V LNMO, 1:1.1 LiFSI/DMC) [64]. The linear sweep voltammograms conducted with a three electrode cell (platinum as working and Li metal as counter and reference electrodes) (Fig. 5e) support these previous reports, as both 1.0 m and 3.25 m LiFSI–SL electrolytes show decomposition current densities below 0.02 mA cm^{-2} beyond 5 V as compared to the 1.2 m $LiPF_6$ (EC/EMC 3:7, Gen II) baseline, which approaches this threshold at platinum electrode potentials as low as 4.4 V vs. Li/Li^+.
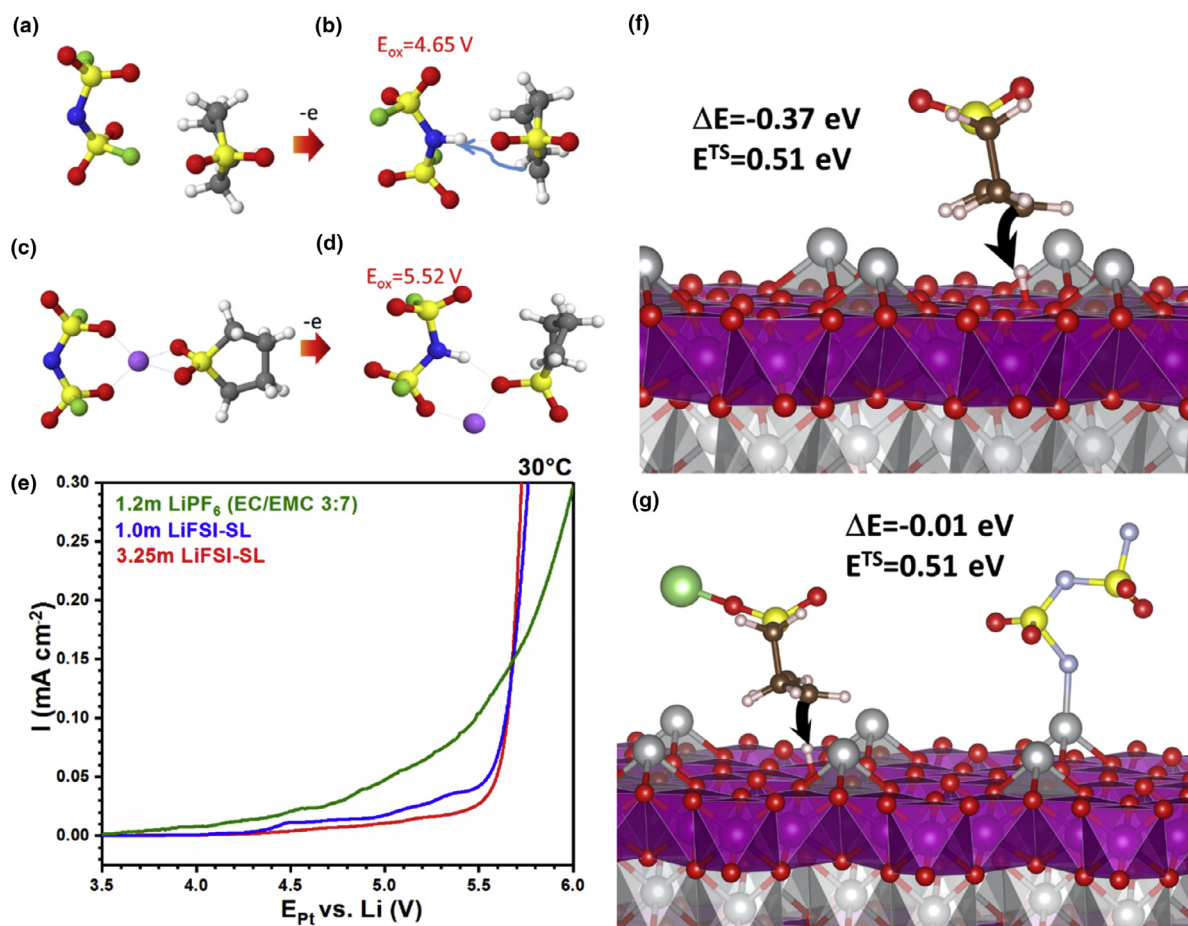
FIGURE 5

Oxidation potential (E_{ox}) (vs. Li/Li$^+$) from G4MP2 QC calculations with clusters surrounded by SMD(SL) implicit solvent model. (a–d) Additional oxidation reactions are shown in Fig. S15 and S15. H-transfer reaction from SL (e) and Li-SL separated from FSI (f) to the Ni$_{0.5}$Mn$_{1.5}$O$_4$ cathode surface from PBE + U DFT calculations. ΔE and E^{TS} are the H-transfer reaction energy and barrier, respectively.

QC calculations predicted the oxidation stability of the SL (FSI$^-$) complexes, surrounded by implicit solvent with SL parameters, to be 4.65 V vs. Li/Li$^+$ (Fig. 5(a and b)) as a result of H-transfer during oxidation from SL to nitrogen of FSI. This oxidation process is attributed to the initial small peak observed in the LSV around 4.5 V (Fig. 5e). The importance of accounting for the H-transfer during oxidation by cathode surfaces has been previously highlighted for the carbonates and ether/FSI complexes [25,65,66] but does not agree with a previous suggestion [61] that H-transfer does not occur in the SL-based electrolytes. In the concentrated regime when all SL molecules are coordinated by Li$^+$, QC calculations predict that the oxidation potential for the LiFSI–SL complexes significantly increases from 4.6 V to 5.5 V (Fig. 5(c and d)). SL and Li$^+$–SL interactions with the low energy (1 1 1) surface of full-charged Ni$_{0.5}$Mn$_{1.5}$O$_4$ charged cathode were also investigated using DFT calculations as shown in Fig. 5(f and g). The isolated SL molecule was found to undergo H-transfer reaction with a barrier of 0.51 eV and reaction energy of −0.37 eV. While this reaction energy is much smaller than the H-transfer from EC and DMC [66], SL deprotonation is expected to readily occur. When SL is complexed to the Li$^+$ cation, however, the reaction energy is essentially zero. The H-transfer reac-

tion leads to a weakening of the bonds between surface oxygen atoms and the sub-surface Mn ions [67]. Such a weakening of Mn—O bonds may facilitate the transition metal dissolution largely responsible for the severe capacity fade common to the high-voltage LNMO cathode. DFT results explain the reasons behind the suppression of the oxidation current for the 3.25 m LiFSI–SL when compared to 1 m LiFSI–SL, because the former has a dramatically smaller fraction of free solvent (Fig. 2). It is worth noting that the fraction of free solvent in direct contact with cathode and conductive additive is expected to be even lower than the 13% found in bulk 3.25 m electrolyte because at high salt concentration, anions such as FSI or TFSI adsorb on the positively charged electrode and screen solvent from direct interaction with electrode, further improving electrolyte stability [68–70]. After establishing that the SL(—H) radical is the first step of LiFSI–SL oxidation reaction on both carbon conductive additive and active electrode, the most probable reactions that follow for the SL(—H) radical were examined using QC (Fig. 6). The S—C bond breaking is expected to be a slow ring opening reaction with a barrier TS1 of 0.69 eV and reaction energy of essentially zero. Critically, the SO$_2$-detachment (M3 complex) after ring opening of SL(—H)• is not energetically favorable, thus no gas-

eous products are expected to form as a result of the single oxidation of SL–FSI. This is in sharp contrast to carbonate molecules, which produce energetically favorable oxidation products that lead to the CO_2 generation [71,72] starting around 4.5 V vs. Li/Li$^+$ when doped with $LiPF_6$ according to QC calculations [25,73]. The SO_2 generation would occur only after SL(—H). radical undergoes another oxidation (M1 → M4 reaction) and overcome a significant barrier for ring opening of TS3 = 0.93 eV. When the SL(—H). radicals are generated they are primarily surrounded by SL molecules. QC calculations predict that the SL(—H). + SL propagation reaction (M6 → M7) that is essentially isoenergetic, while the SL(—H). + SL(—H). termination reactions (M8 → M9, M8 → M10, M8 → M11) are very energetically favorable, but are limited by low concentration of the SL(—H). radicals compared to SL molecules. Thus, we conclude that SL oxidation

is expected to result in a slow polymerization, which effectively passivates the cathode surface with low gas-generation unlike EC-based electrolytes.

Full cell performance and the cathode electrolyte interphase (CEI)

LNMO presents an operating voltage that exceeds the anodic stability of most carbonate-based electrolytes. To rigorously confirm the high voltage stability of SL–LiFSI electrolytes observed in the anodic linear sweep voltammetry measurements, full Li-ion cells constructed with LNMO–MCMB configuration were assembled and tested. The advantage in stability of the concentrated LiFSI–SL system is quite obvious at elevated temperatures, as shown in Fig. S20, which features a deliberately strenuous
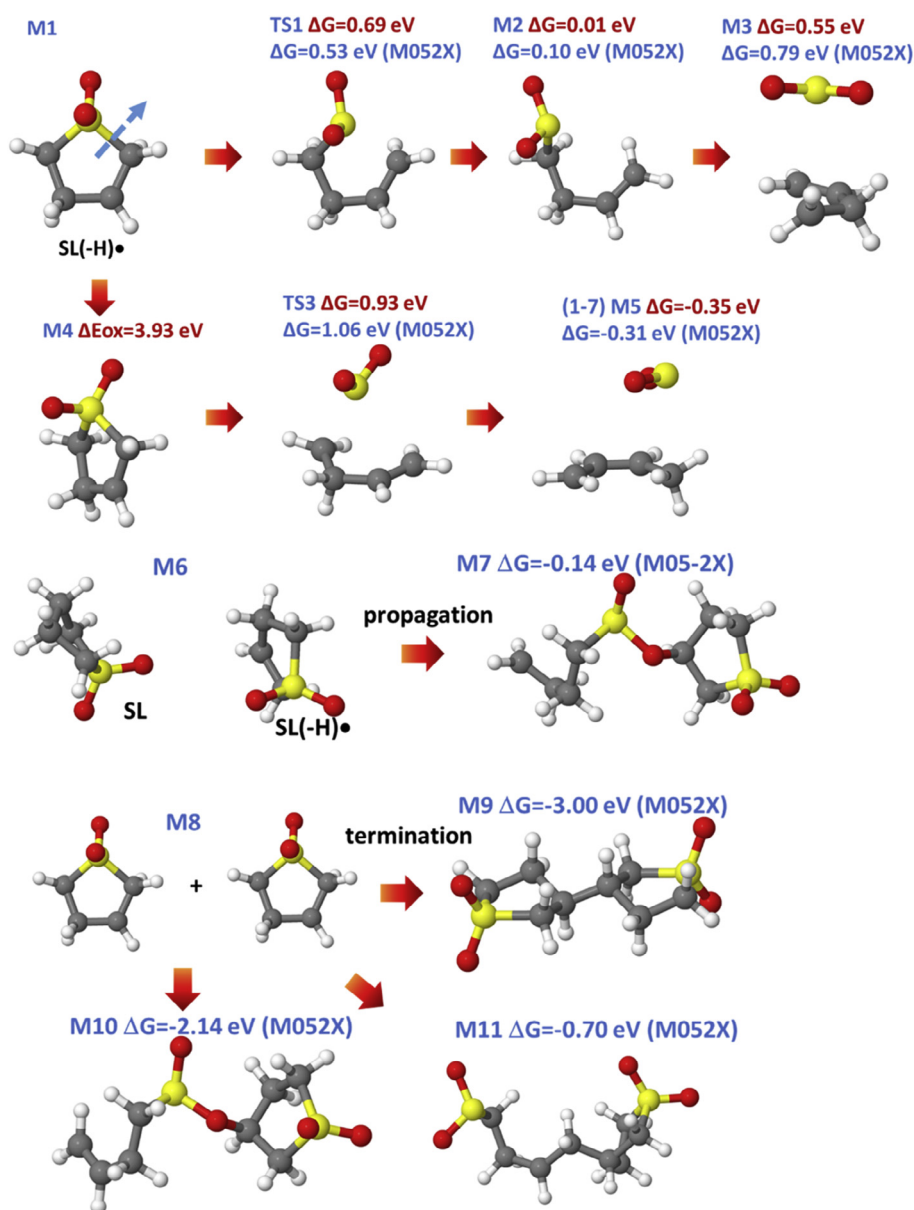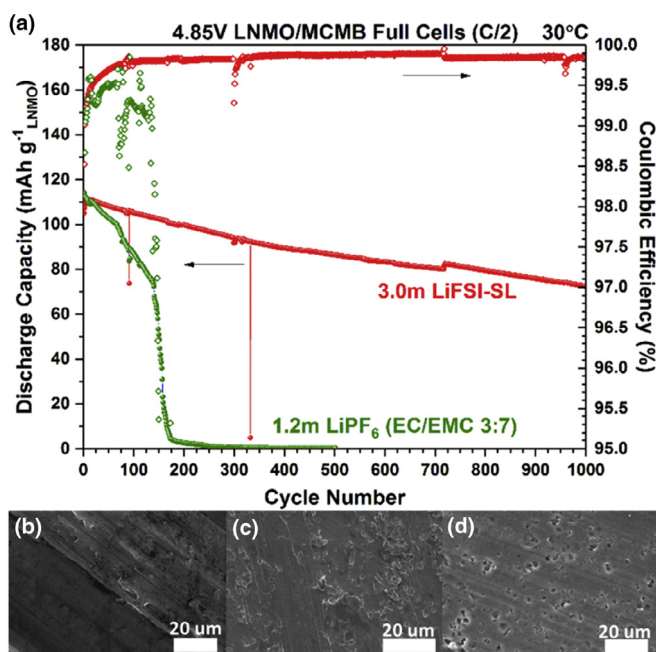

FIGURE 6

The SL(—H) ring opening, oxidation, propagation with SL and termination reaction from G4MP2 calculations (in red) and M05-2X/6-31+G(d,p) (in blue). Each complex was immersed in implicit solvent modeling using SMD(SL) model.

cycling protocol at 55 °C including two long duration formation cycles at C/20, followed by cycling at C/5. Under these aggressive cycling conditions, the baseline carbonate stability is completely compromised, yielding only a single cycle with little discharge capacity, while the LiFSI–SL system maintains more than 50% of its original discharge capacity after more than 90 cycles. The combination of high voltage (4.85 V cutoff) and high temperature (55 °C) makes this a significant stability demonstration for an additive-free, two component electrolyte. Galvanostatic cycling at room temperature (Fig. 7a) indicates that the baseline electrolyte (Gen II) suffers a severe decline in capacity starting around 150 cycles, while the high concentration 3 m LiFSI–SL system exhibits relatively stable capacity retention with minor losses up until the cell cycling was stopped at the 1000th discharge for characterization, at which point it still retained 69% of the original first cycle discharge capacity.

In an effort to diagnose the source of capacity loss in the LiFSI–SL system, the cathode's aluminum current collector was imaged with SEM at different points in cycling (pristine (Fig. 7b), 50th discharge (Fig. 7c), and after 1000 cycles (Fig. 7d), yielding multiple interesting results. Despite minimal pitting in the pristine current collector and after the 50th discharge (Fig. 8b and c, respectively), significant Al pitting is evident after long duration cycling (Fig. 8d). This result challenges an established notion in the field that high concentration LiFSI-based electrolytes are able to mitigate Al corrosion [64,74], instead suggesting that the reaction kinetics are sufficiently suppressed to an extent that these corrosion reactions are not necessarily observable in CV sweeps [75] or after short

cycling durations. While this could be related to sulfolane's relatively high dielectric constant (43.3 @ 30 °C), which may initially subdue precipitation of compounds such as AlF_3 [76], at high concentrations the availability of free solvent is minimized. Whether this long term observation of corrosion applies solely to LiFSI or to other concentrated fluorosulfonylimide salt systems [77] requires further investigation via long term cycling and microscopy studies. One other point of note is the stark difference in the condition of the current collector on the side loaded with the active material vs. the backside (bare Al). Comparison of SEM images from these surfaces (Fig. S21) shows that the side with the active material undergoes significantly more corrosion/pitting than the backside, which suggests two possibilities. The first is that the electrolyte has wetted the active material and is readily available for continued surface reactions on the loaded side, but less electrolyte is locally available to sustain continuous reactions on the backside. The second is the species generated at the CEI may contribute to the corrosion process, and these surface reactions occur faster where a higher concentration of these products are immediately present. While the specific mechanism is beyond the focus of this work, it is certainly an interesting topic for further study.

In a separate study, the cathode-electrolyte interphase (CEI) structure and chemistry were characterized with EELS, XPS, and cryo-(S)TEM, which was used to preserve CEI structure/-chemistry and avoid beam damage). After the 50th discharge, the CEI structure of the carbonate baseline, shown in Fig. 8a, exhibits significant variations in thickness and uniformity, with open sections of minimal coverage allowing direct exposure of the electrolyte to the cathode particle surface ((133) plane in this case) as well as significantly thicker sections (see Fig. S22). Conversely, the CEI generated on the LNMO particle ((226) plane) after 50 cycles with the 3 m LiFSI–SL appears much more uniform in thickness and conformal in surface coverage (Figs. 8b, S23). This is in approximate agreement regarding thickness with another CEI study, albeit for a different cathode material and lower voltage cutoff [78]. The difference in the shape of the oxygen K-edge at ~535 eV energy loss in Fig. 8c and d is attributed to either an excess surface metal concentration (cation interstitials) [79] or due to oxygen vacancy formation at the LNMO surface in the carbonate baseline, which is known to destabilize the material and increase the likelihood of transition metal migration [80]. Additionally, the L_3/L_2 intensity ratio of Mn increases from 2.2 in LiFSI–SL to 2.8 in the carbonate baseline (Fig. S25), suggesting a significant surface concentration of reduced Mn^{3+}, resulting in local Jahn–Teller distortion [81]. XPS analysis of O1s peak of the CEIs after the 40th discharge shows suppression of the TM—O signal for both electrolytes (Fig. 8e and f), supporting the presence of a surface film as compared to the pristine electrode, but this suppression effect is particularly strong for the LiFSI-SL system, reiterating the presence of a dense, conformal, CEI as demonstrated by TEM. Lastly, the S—O signature observed with XPS as well as the S L-edge observed in EELS (Fig. S24) for the CEI both endorse the QC predictions of polymerization and termination of a sulfur-based cathode surface film.

FIGURE 7

Galvanostatic cycling capacity for Gen II and 3 m LiFSI-SL at 30 °C. Figures (b–d) show the Al current collector corrosion on the active material side of the current collector for the 3 m LiFSI-SL cells with (b) pristine, (c) 50th discharge, (d) 1000th discharge.
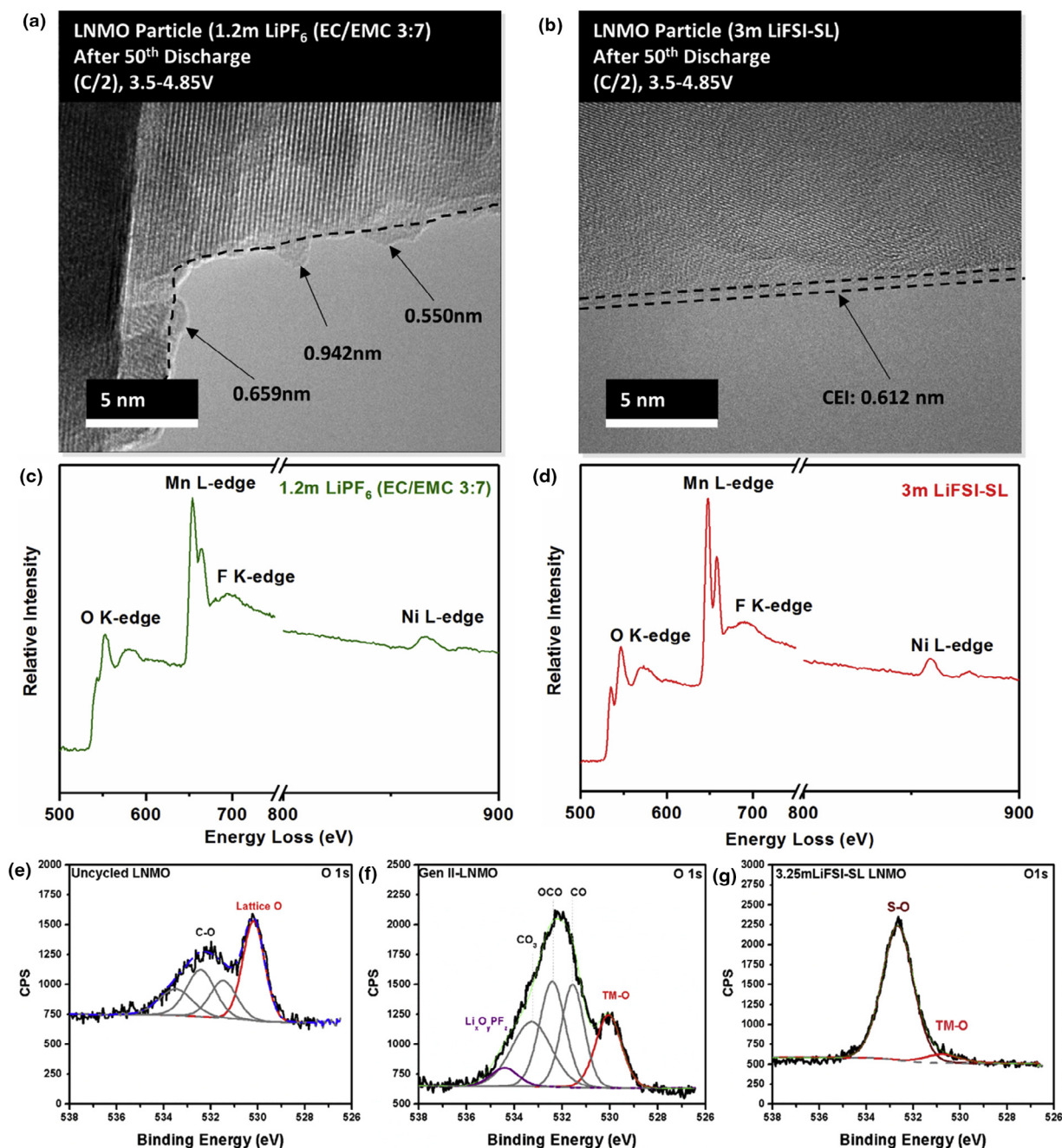
FIGURE 8

Cryo-TEM images and EELS spectra of LNMO particle CEI after 50th discharge with 1.2 m $LiPF_6$ (EC/EMC 3:7) (a, c) and 3 m LiFSI-SL (b, d). XPS of pristine cathode surface (e), Gen-II CEI (f), and 3.25 m LiFSI-SL CEI (g) after 40th discharge.

Conclusion

In this work we introduce a new carbonate-free electrolyte system that offers a promising new pathway toward enabling aggressive battery chemistries that carbonate-based electrolytes have failed to support. The electrolyte consisting of high concentration LiFSI dissolved in SL forms an SEI highly enriched with LiF and Li_2O, which support reversible Li^+-intercalation behavior across all concentrations tested, reversing the previous failures of SL electrolytes on graphitic anode. At the cathode–electrolyte interface, significant anodic stability is attributed to the high oxidation potential of SL complexed with Li^+ and the polymeriza-

tion of SL. Combining these merits, this system demonstrated excellent high voltage and high temperature stability in full Liion cells constructed with graphite and high-voltage LMNO, opening the door to future carbonate-free electrolyte design and further optimization.

Material and methods
Experimental
Electrolyte preparation

The electrolytes were prepared using LiFSI (Oakwood Products, Inc.-battery grade), $LiPF_6$ (BASF-battery grade), propylene carbon-

ate (PC, BASF-battery grade), ethylene carbonate (EC, BASF-battery grade), ethylmethyl carbonate (EMC, BASF-battery grade), and tetramethylene sulfone (SL, Sigma Aldrich-98% purity). Given the quality of the sulfolane (SL) and its slightly yellow-brown color, it was purified [82]. The resulting material is a sticky white solid at room temperature that melts at 28.6 °C to form a clear liquid. The carbonate solvents (PC, EMC, EC) were dried using molecular sieves and the salts were dried under vacuum at 60 C for 12 h to remove any residual water. Seven salt-solvent electrolyte compositions were used in this work: 1.0 m LiFSI–SL, 3.0 m LiFSI-SL, 3.25 m LiFSI–SL, 1.0 m LiPF$_6$–SL, 1.0 m LiFSI–PC, 4.0 m LiFSI–PC, and 1.2 m LiPF$_6$ EC: EMC (3:7 wt%) (all formulated in the glovebox).

Electrolyte characterization

Electrolyte conductivity κ of the electrolytes was measured with an Agilent E4980A precision LCR meter at selected temperatures within a Tenney Jr. environmental chamber, controlled and automated with an in-house computer program. The conductivity cells consist of a pair of platinum–iridium electrodes and a Pyrex cell body that can be sealed with a ground-glass stopper. The cell constants of a nominal value of 0.1 cm^{-1} were calibrated with a standard KCl solution of 111 mS cm^{-1} nominal value. The temperature measurements ranged from 85 to −20 °C in 5 K decrement, stopping at each for an hour of thermal equilibration before taking a measurement. After the measurement at a set temperature, readings from five thermocouples placed near the conductivity cells were recorded and averaged to give the actual temperature for the conductivity values. Each conductivity measurement consisted of an impedance scan from 20 Hz to 2 MHz with an amplitude of 10 mV, from which a Z′Z″ plot was made and κ was evaluated from the impedance curve. This followed parameters from our previous publication [83].

Graphite half cell experiments

The graphite electrodes contained 91.83% Gelon G15 MCMB with 2 wt% C45 conductive additive and 6 wt% Kureha 9300 binder, and were coated on 10-μm-thick Cu foil. These electrodes were provided by the CAMP Facility at Argonne National Laboratory. These electrodes were punched to 9/16″ diameter (1.6 cm^2 area) and assembled in 2032 coin cells (Hohsen Corp.) with Celgard 3501 separators soaked in various electrolytes (1 m, 3.25 m LiFSI SL, 1 m LiPF$_6$ SL, and 1.2 m LiFSI ethylene carbonate (EC): ethylmethyl carbonate (3:7 wt%)) and a 1.5- mm-thick, 0.5″ diameter Li metal counter-electrode (FMC Corp.). Cell assembly was carried out in a dryroom (dew point <−75 °C). After resting for 12 h, the coin cells were cycled in a 30° environmental chamber with a Maccor battery cycler. The galvanostatic cycling protocol included upper and lower voltage limits of 2.0 V and 0.05 V, respectively, for a formation cycle at C/20 followed by 4.5 cycles at C/5 until the end of the sixth discharge (lithiated graphite). Cells that exhibited exfoliation/decomposition behavior without reaching the lower limit (i.e., 1.0 m PF$_6$ PC) were discharged at C/20 for 80 h for consistency in the XPS analysis. The cell configuration was also used for cyclic voltammetry experiments on Solartron potentiostat. Here the Li metal acts as the counter electrode and reference electrode, while MCMB anode is the working electrode. The experimental parameters included

sweeping the voltage from OCV to 0.05 V at 0.05 mV s^{-1}, for a total of three CV cycles.

Full cell experiments

The LiMn$_{1.5}$Ni$_{0.5}$O$_4$ electrodes contained 84% Gelon G15 MCMB with 8 wt% C45 conductive additive and 8 wt% Kureha 1120 binder, and were coated on Al foil. These electrodes were provided by the CAMP Facility at Argonne National Laboratory. These electrodes were punched to 9/16″ diameter (1.6 cm^2 area) with a areal loading of 14.7 mg cm^{-1} and assembled versus MCMB anode with a mass loading of 6.44 mg cm^{-1} in 2032 coin cells (Hohsen Corp.) with glass fiber (Whatman QMF) separators soaked in various electrolytes (3.25 m LiFSI SL, and 1 m LiPF$_6$ SL, 1.2 m LiPF$_6$ EC: EMC (3:7 wt%). Cell assembly was carried out in a dryroom (dew point <−75 °C). After resting for 12 h, the coin cells were cycled in a 30 °C and 55 °C environmental chamber with a Maccor battery cycler. The galvanostatic cycling protocol included upper and lower voltage limits of 4.85 V and 3.5 V, respectively, for a two formation cycles at C/20 followed by 300 cycles at C/5.

Linear sweep voltammetry

The experiment was conducted using a three electrode Swagelok cell containing Li metal as the counter and reference electrode, with the platinum metal disc (0.5-mm diameter) as the working electrode. The glass fiber separator (Whatman QMF) helps avoid the cell from shorting, with 300 μL of electrolyte. Experiments were carried out on a single-channel Gamry Potentiostat (Reference 3000), sweeping from OCV to 6 V at 2 mV s^{-1}. Experiments were conducted three times for each electrolyte to ensure reproducibility.

Cyclic voltammetry and impedance measurements

The experiment was conducted in a two electrode coin cell with the MCMB graphite anode as the working electrode and the Li metal as the reference/counter electrode. The cell was measured from OCV to 0.05 V at 0.05 mV s^{-1} for three scans using Solartron 1287 potentiostat at room temperature.

Impedance measurements were measured in the same coin cell using a Gamry Potentiostat (Reference 3000). The MCMB half cells were first lithiated at C/20 until 0.05 V and left to rest for four hours until the cells reached OCV. The impedance was measured using 10 mA AC potential from 0.1 Hz to 1 MHz versus open circuit potential. The cells were then delithiated at the C/20 until 2 V. The cell was allowed to reach OCV and the impedance measurement was taken. After the impedance measurements were taken, an equivalent circuit model was fit to the data to analyze the reactions that took place using Z view software (v. 3.4a, Scribner Associates, Inc.).

XPS sample preparation/analysis

Following cycling, all coin cells were disassembled in an argon-filled Vacuum Atmospheres Nexus One glovebox (H$_2$O < 1 ppm, O$_2$ < 1 ppm). The electrodes were rinsed with anhydrous dimethyl carbonate and dried in vacuum at room temperature to evaporate any residual solvent. The samples were transferred to a PHI Versaprobe III XPS system using a sealed vacuum transfer capsule enabling rigorous air/moisture exclusion, so the electrode surface chemistry is believed to be unaltered. The XPS was

operated using Al anode source at 15 kV with a 100-μm × 100-μm spot size and charge compensation was provided by the PHI charge neutralization system to eliminate differential charging. Survey scans were collected with a pass energy of 224 eV and a 1.0 eV step size followed by high-resolution scans with a pass energy of 26 eV and a step size of 0.05 eV. Peak fitting was performed using CasaXPS software (version 2.3.15, Casa Software Ltd.), using 70/30 Gaussian/Lorentzian line shapes on a linear background. Quantification was performed using peak area corrections to account for the photoionization cross section of each element and the instrument geometry. All spectra were shifted relative to the binding energy of the carbon 1 s sp^3 (assigned to 284.5 eV) to compensate for any off-set during the measurement.

Infrared spectroscopy

All FTIR spectra were collected in an attenuated total internal reflection (ATR) geometry using a Nicolet 6700 (Thermo Scientific) spectrometer with a diamond ATR assembly (single bounce, 45°, Specac Ltd.). All spectra were the average of 64 scans collected at a resolution of 2 cm^{-1}. LabSpec5 curve fitting software was used to fit spectra to mixed Gaussian-Lorentzian functions.

Cryo-(S)TEM and EELS

After cycling, all coin cells were disassembled in an argon-filled glove box. The cathode was rinsed with DMC to remove trace Li salt and dispersed on TEM lacey carbon grid. The loading and transferring the grid to TEM were carefully controlled to prevent sample from air exposure and detail information can be found in our previous publication [84]. TEM was recorded on a field emission gun JEOL-2800 at 200 kV with Gatan OneView Camera (full 4 K × 4 K resolution). STEM-EELS was performed on JEOL JEM-ARM300CF at 300 kV, equipped with double correctors. EELS spectra shown in this work were acquired from a square area of ∼3 × 3 nm near CEI layer with an acquisition time of 1 s. To minimize possible electron beam irradiation effects, EELS spectra presented in this work were acquired from areas without pre-beam irradiation. Mn L$_3$ to L$_2$ intensity ratio analysis was done by averaging over 10 spectra using the method described by Wang et al. [85]. Note that (S)TEM–EELS was carried out under cryogenic temperature (∼180 °C) to minimize beam damage influence on CEI structure/chemistry.

Computational methods
Molecular modeling

QC calculations were performed using the g09 Gaussian package [59]. An implicit solvent SMD solvation model with SL parameters (ε = 42.5, ε$_\infty$ = 2.194) was employed in all calculations. The composite methodology G4MP2 was utilized for small complexes because it was previously demonstrated to accurately predict ionization energies, electron and proton affinities and enthalpies of formation with the mean absolute deviations of 0.73–1.29 kcal/mol [60]. Less expensive M05-2X/6-31+G(d,p) density functional theory (DFT) calculations were performed for examining the reactions in larger complexes for which G4MP2 is too computationally expensive. Oxidation and reduction potentials were calculated according to Eq. (2) and (3), in which the value of the potential vs. an electron at rest in vacuum was converted to the Li/Li$^+$ scale by subtraction of 1.4 V as previ-

ously discussed [61]. The shift factor of 1.4 V depends on the nature of the solvent and salt concentration giving rise to uncertainty of 0.1–0.3 V for predicted values [61].

$$E^0_{oxidation}(M) = [\Delta G_e + \Delta G^0_S(M^+) - \Delta G^0_S(M)]/F - 1.4 \quad (2)$$

$$E^0_{reduction}(M) = -[\Delta G_e + \Delta G^0_S(M^-) - \Delta G^0_S(M)]/F - 1.4 \quad (3)$$

where ΔG_e is the ionization free energy or electron affinity in gas-phase at 298.15 K; $\Delta G_S(M^+)$, $\Delta G_S(M^-)$ and $\Delta G_S(M)$ are the free energies of solvation of the oxidized, reduced and initial complexes, respectively, and F is the Faraday constant.

Details of DFT calculations of SL deprotonation reaction on the fully charged Ni$_{0.5}$Mn$_{1.5}$O$_4$ cathode surface and molecular dynamics simulation methodology are described in Supporting information.

Data availability

The raw/processed data required to reproduce these findings cannot be shared at this time due to technical or time limitations—the data also form part of an ongoing study.

Appendix A. Supplementary data

Supplementary data associated with this article can be found, in the online version, at https://doi.org/10.1016/j.mattod.2018.02.005.

References

[1] E. Peled, J. Electrochem. Soc. 126 (1979) 2047–2051.
[2] K. Xu, Chem. Rev. 104 (2004) 4303–4417.
[3] K. Xu, Chem. Rev. 114 (2014) 11503–11618.
[4] R. Fong, U. von Sacken, J.R. Dahn, J. Electrochem. Soc. 137 (1990) 2009–2013.
[5] J. Xia et al., J. Power Sources 328 (2016) 124–135.
[6] J. Xia et al., J. Electrochem. Soc. 163 (2016) A1637–A1645.
[7] D. Chalasani et al., J. Power Sources 208 (2012) 67–73.
[8] B. Li et al., Electrochem. Commun. 17 (2012) 92–95.
[9] G.B. Han et al., J. Power Sources 195 (2010) 3709–3714.
[10] A. Manthiram, K. Chemelewski, E.S. Lee, Energy Environ. Sci. 7 (2014) 1339–1350.
[11] J. Demeaux et al., Electrochim. Acta 89 (2013) 163–172.
[12] N.P.W. Pieczonka et al., J. Phys. Chem. C 117 (2013) 15947–15957.
[13] M.Q. Xu et al., J. Phys. Chem. C 118 (2014) 7363–7368.
[14] J. Chen et al., J. Power Sources 303 (2016) 41–48.
[15] A. Jarry et al., J. Am. Chem. Soc. 137 (2015) 3533–3539.
[16] M.S. Ding et al., J. Electrochem. Soc. 148 (2001) A1196–A1204.
[17] S. Zugmann et al., Electrochim. Acta 56 (2011) 3926–3933.
[18] A.V. Cresce et al., Phys. Chem. Chem. Phys. 19 (2017) 574–586.
[19] F.F. Chen, M. Forsyth, Phys. Chem. Chem. Phys. 18 (2016) 19336–19344.
[20] G.A. Giffin et al., J. Power Sources 342 (2017) 335–341.
[21] D.M. Seo et al., J. Electrochem. Soc 160 (2013) A1061–A1070.
[22] J.E. Katon, W.R. Feairheller, Spectrochim. Acta 21 (1965) 199–201.

[23] X. Xuan et al., Spectrochim. Acta, Part A Mol. Biomol. Spectrosc. 57 (2001) 1555–1560.
[24] D.M. Seo et al., J. Electrochem. Soc 159 (2012) A553–A565.
[25] F. Wu, O. Borodin, G. Yushin, MRS Energy Sustain. 4 (2017) 1–15.
[26] K. Xu, C.A. Angell, J. Electrochem. Soc. 149 (2002) A920–A926.
[27] K. Xu, A. von Cresce, J. Mater. Chem. 21 (2011) 9849–9864.
[28] X.G. Sun, C.A. Angell, Electrochem. Commun. 11 (2009) 1418–1421.
[29] M. Nie et al., J. Phys. Chem. C 117 (2013) 25381–25389.
[30] Y. Pan, G.L. Wang, B.L. Lucht, Electrochim. Acta 217 (2016) 269–273.
[31] K. Xu, J. Electrochem. Soc. 156 (2009) A751–A755.
[32] K. Tasaki, A. Goldberg, M. Winter, Electrochim. Acta 56 (2011) 10424–10435.
[33] J.O. Besenhard et al., J. Power Sources 54 (1995) 228–231.
[34] M.R. Wagner et al., Electrochem. Commun. 7 (2005) 947–952.
[35] L. Xing et al., Acc. Chem. Res. (2018).
[36] D. Shanmukaraj et al., ChemSusChem 8 (2015) 2691–2695.
[37] G.C. Chung et al., J. Electrochem. Soc. 147 (2000) 4391–4398.
[38] K. Leung, Phys. Chem. Chem. Phys. 17 (2015) 1637–1643.
[39] T. Kawaguchi et al., J. Power Sources 271 (2014) 431–436.
[40] S.A. Delp et al., Electrochim. Acta 209 (2016) 498–510.
[41] L. Suo et al., Adv. Energy Mater. (2017) 1701189.
[42] Y. Yamada et al., J. Am. Chem. Soc. 136 (2014) 5039–5046.
[43] Y. Yamada et al., ACS Appl. Mater. Interfaces 6 (2014) 10892–10899.
[44] K. Edström, M. Herstedt, D.P. Abraham, J. Power Sources 153 (2006) 380–384.
[45] P. Verma, P. Maire, P. Novák, Electrochim. Acta 55 (2010) 6332–6341.
[46] H. Tamura et al., Electroanal. Chem. (1992) 333.
[47] H. Bryngelsson et al., J. Power Sources 174 (2007) 970–975.
[48] I.W. Doron Aurbach, A. Schechter, H. Cohen, Langmuir (1996).
[49] P. Lu et al., J. Phys. Chem. C 118 (2014) 896–903.
[50] W. Gu et al., Adv. Funct. Mater. 26 (2016). 1490-1490.
[51] I.A. Shkrob et al., J. Phys. Chem. C 118 (2014) 19661–19671.
[52] A. Budi et al., J. Phys. Chem. C 116 (2012) 19789–19797.
[53] M. Nie, B.L. Lucht, J. Electrochem. Soc. 161 (2014) A1001–A1006.
[54] B. Philippe et al., J. Am. Chem. Soc. 135 (2013) 9829–9842.
[55] O. Borodin et al., ECS Trans. 69 (2015) 113–123.
[56] L.E. Camacho-Forero, T.W. Smith, P.B. Balbuena, J. Phys. Chem. C (2016).
[57] H. Kim et al., Adv. Energy Mater. 5 (2015).
[58] V.S. Kolosnitsyn, L.V. Sheina, S.E. Mochalov, Russ. J. Electrochem. 44 (2008) 575–578.
[59] S.Y. Lee, K. Ueno, C.A. Angell, J. Phys. Chem. C 116 (2012) 23915–23920.
[60] A. Abouimrane, I. Belharouak, K. Amine, Electrochem. Commun. 11 (2009) 1073–1076.
[61] Y. Wang et al., J. Phys. Chem. Lett. 4 (2013) 3992–3999.
[62] L.D. Xing et al., Electrochim. Acta 133 (2014) 117–122.
[63] O. Borodin, W. Behl, T.R. Jow, J. Phys. Chem. C 117 (2013) 8661–8682.
[64] J. Wang et al., Nat. Commun. 7 (2016) 12032.
[65] O. Borodin, W. Behl, T.R. Jow, J. Phys. Chem. C 117 (2013) 8661–8682.
[66] O. Borodin et al., Nanotechnology 26 (2015) 354003.
[67] K. Leung, Chem. Mater. 29 (2017) 2550–2562.
[68] J. Vatamanu, O. Borodin, J. Phys. Chem. Lett. (2017) 4362–4367.
[69] C. Yang et al., Joule 1 (2017) 122–132.
[70] O. Borodin et al., Acc. Chem. Res. 50 (2017) 2886–2894.
[71] L. Xing, O. Borodin, Phys. Chem. Chem. Phys. 14 (2012) 12838–12843.
[72] Y.T. Wang et al., Phys. Chem. Chem. Phys. 16 (2014) 6560–6567.
[73] O. Borodin, Molecular modeling of electrolytes, in: T.R. Jow, K. Xu, O. Borodin, M. Ue (Eds.), Electrolytes for Lithium and Lithium-Ion Batteries, Springer, New York, 2014, pp. 371–401.
[74] Y. Yamada et al., ChemElectroChem 2 (2015) 1687–1694.
[75] D.W. McOwen et al., Energy Environ. Sci. 7 (2014) 416–426.
[76] X. Wang, E. Yasukawa, S. Mori, Electrochim. Acta 45 (2000) 2677–2684.
[77] K. Matsumoto et al., J. Power Sources 231 (2013) 234–238.
[78] Y. Qian et al., J. Power Sources 329 (2016) 31–40.
[79] H. Shiiba et al., J. Phys. Chem. C 119 (2015) 9117–9124.
[80] D. Qian et al., PCCP 16 (2014) 14665–14668.
[81] K.J. Carroll et al., PCCP 15 (2013) 11128–11138.
[82] K. Xu, C.A. Angell, J. Electrochem. Soc. 145 (1998) L70–L72.
[83] M.S. Ding, A. von Cresce, K. Xu, J. Phys. Chem. C 121 (2017) 2149–2153.
[84] X. Wang et al., Nano Lett. 17 (2017) 7606–7612.
[85] Z.L. Wang, J. Bentley, N.D. Evans, Micron 31 (2000) 355–362.